Journal of Catalysis 275 (2010) 1–10

Contents lists available at ScienceDirect

Journal of Catalysis

journal homepage: www.elsevier.com/locate/jcat

Structure and properties of $PVMo_{11}O_{40}$ heteropolyoxomolybdate supported on silica SBA-15 as selective oxidation catalyst

T. Ressler *, U. Dorn, A. Walter, S. Schwarz, A.H.P. Hahn

Technische Universität Berlin, Institut für Chemie, Sekr. C2, Strasse des 17. Juni 135, D-10623 Berlin, Germany

ARTICLE INFO

Article history:
Received 20 April 2010
Revised 29 June 2010
Accepted 1 July 2010
Available online 17 August 2010

Keywords:
Heterogeneous catalysis
Structure–activity relationships
EXAFS spectroscopy
Molybdenum
Oxides
Keggin
$PVMo_{11}O_{40}$
SBA-15
Selective
Oxidation

ABSTRACT

Investigations into structure and properties of heteropolyoxomolybdates (HPOM) supported on nanostructured silica SBA-15 for the selective oxidation of propene are presented. $H_4[PVMo_{11}O_{40}]$ Keggin ions supported on SBA-15 ($PVMo_{11}$-SBA-15) were prepared by incipient wetness of silica SBA-15 with suitable precursor solutions. Structure and properties of the resulting material were studied ex situ by X-ray diffraction and nitrogen physisorption measurements and in situ by combined X-ray absorption spectroscopy (XAS) and mass spectrometry under various reaction conditions. The characteristic structure of $PVMo_{11}$-SBA-15 and its evolution under reactive gas atmosphere are compared to that of bulk $H_4[PVMo_{11}O_{40}]\cdot xH_2O$. Structural investigations of as-prepared $PVMo_{11}$-SBA-15 have shown that the respective Keggin ions can be readily supported on silica SBA-15. In situ XAS measurements under reducing or oxidizing conditions revealed a pronounced support interaction effect. This effect resulted in a further decreased thermal stability of the supported Keggin ions compared to bulk $H_4[PVMo_{11}O_{40}]\cdot xH_2O$. Apparently, no stable HPOM Keggin ions could be obtained on silica SBA-15 under reaction conditions. However, in spite of their low thermal stability, HPOM supported on SBA-15 remain suitable well-defined precursors for preparing mixed oxide model catalysts for selective oxidation reactions.

1. Introduction

Molybdenum oxide catalysts selectively oxidize light alkenes and alkanes with gas phase oxygen [1,2]. Addition of V, W, Nb, or Te results in the formation of mixed oxide catalysts with various characteristic structures (e.g. $(MoVW)_5O_{14}$ [3] and MoVNbTe oxides [4–6]). Compared to α-MoO_3, these mixed oxides exhibit much higher activity and selectivity [7,8]. With respect to structure–activity relationships, introduction of additional metal centers like V or W to MoO_x catalysts indeed improves the catalytic performance of the resulting mixed oxides [1,2]. However, this approach simultaneously alters chemical composition and geometric and electronic structure. Hence, it becomes difficult to disentangle compositional and structural effects. Therefore, the superior performance of mixed oxide catalysts cannot unambiguously be ascribed to the functionality of the additional metal centers (chemical complexity) or a particular structural motif (structural complexity). This question needs to be resolved to understand the functionality of molybdenum-based catalysts and to develop new and improved catalysts.

Further addressing this predicament requires suitable model systems with either plain composition and structural variety, or structural invariance and suitable compositional variety. On the one hand, α-MoO_3 and stabilized hexagonal MoO_3 [9], for instance, are model systems with the same composition and structural variety. On the other hand, Keggin type heteropolyoxo molybdates (HPOM) are suitable materials that possess compositional flexibility and structural invariance. HPOM (e.g. $H_3[PMo_{12}O_{40}]$) are active catalysts for heterogeneous selective oxidation reactions [10–13]. HPOM are particularly suited to accommodate additional metal centers while maintaining the basic structural motif of the parent Keggin ion. Therefore, HPOM have been frequently employed as model systems for studying the structural evolution of molybdenum-based mixed oxide catalysts under reaction conditions [14–16].

In addition to using bulk model catalysts for determining structure activity relationships, supported metal oxide catalysts have received increasing attention [17–20]. Supported oxide catalysts exhibit high dispersion and an improved surface to bulk ratio. Hence, the intrinsic problem of bulk sensitive techniques to distinguish between accessible metal sites at the surface and metal centers buried in the bulk can be avoided. Therefore, relating a particular structure of a supported catalyst under reaction conditions to its catalytic performance will be more reliable. Nanostructured SiO_2 materials such as silica SBA-15 [21,22] are suitable support systems for oxide catalysts [23–26]. They possess a large surface area, a homogeneous internal pore structure, and moderately interact with the oxide catalyst.

* Corresponding author. Fax: +49 30 314 21106.
E-mail address: thorsten.ressler@tu-berlin.de (T. Ressler).

0021-9517/$ - see front matter © 2010 Elsevier Inc. All rights reserved.
doi:10.1016/j.jcat.2010.07.001

Industrial applications and investigations of supported tungstate or molybdate heteropoly acids (HPA) have been recently reviewed [27,28]. The authors distinguished between low (<10%) and high loading of HPA and assumed corresponding correlations between structure and properties of HPA. Immobilization of HPA on various support materials and their use as oxidation catalyst was also reviewed by Kim et al. [29]. However, the local structure around the W or Mo centers in the activated catalyst was elucidated in neither study. Newman et al. reported preparation and structural characterization of a series of SiO_2 supported $H_3PW_{12}O_{40}$ catalysts [30]. Structural characterization of the as-prepared materials using X-ray absorption spectroscopy confirmed that the Keggin unit is intact for all loadings studied. Structural evolution of the materials under reaction conditions, however, was not elucidated. In total, studies on structure and properties of HPOM species on suitable supports and, in particular, their structural evolution under reaction conditions remain scarce. Here, we present in situ investigations into the evolution of structure and properties of heteropolyoxomolybdates supported on nanostructured silica SBA-15 for the selective oxidation of propene.

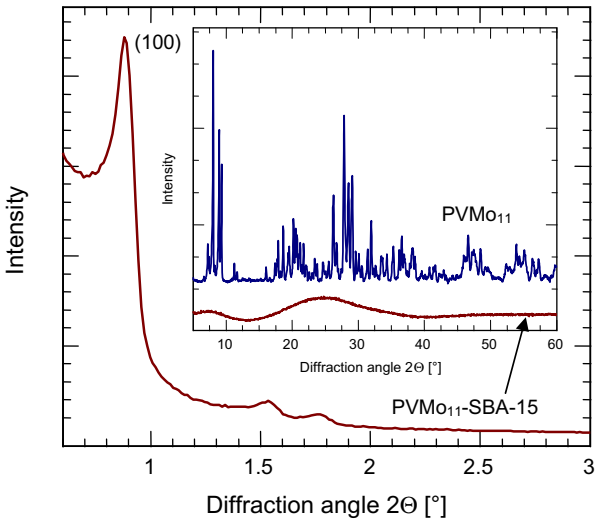

Fig. 1. Small-angle and wide-angle (inset) X-ray diffraction patterns of as-prepared $PVMo_{11}$-SBA-15 and bulk $H_4[PVMo_{11}O_{40}]\cdot 13H_2O$.

2. Experimental

2.1. Sample preparation

Mesoporous silica SBA-15 was prepared according to the literature procedures [23,31]. A concentration of 1.0 g of triblock copolymer (Aldrich, pluronic, P-123) was dissolved in 60.5 ml of water and 3.3 ml of concentrated H_2SO_4 at 323 K. After drop wise addition of 2.3 g of tetraethyl orthosilicate (TEOS), the reaction mixture was stirred for 24 h at 323 K. The resulting suspension was heated in a closed bottle to 381 K for 24 h. The resulting white powder was filtered, washed with deionized water, and dried at 353 K for 72 h. The dry powder was calcined at 453 K for 4 h and, subsequently, at 823 K for 12 h.

HPOM precursors were prepared as follows. 19.72 g MoO_3 (Sigma Aldrich) or 17.89 g MoO_3 and 1.03 g V_2O_5 were dissolved in 650 ml water and heated under reflux to obtain $H_3[PMo_{12}O_{40}]\cdot n$-$H_2O$ or $H_4[PVMo_{11}O_{40}]\cdot 13H_2O$, respectively. A volume of 93 ml of 0.12 molar phosphoric acid was added drop wise to the reaction mixture. The resulting suspension was heated under reflux for 3 h and left 12 h at 298 K until a clear yellow solution was obtained. The remainder was filtered off and the volume of the resulting yellow solution was reduced to ~30 ml using an evaporator. HPOM precursors crystallized during storage at 277 K for several days. Phase purity and structure were confirmed by XRD analysis (Fig. 1).

HPOM supported on silica SBA-15 was prepared via incipient wetness. 228 mg $H_3[PMo_{12}O_{40}]\cdot nH_2O$ or 206 mg $H_4[PVMo_{11}O_{40}]\cdot 13H_2O$ were dissolved in 1.5 ml water to be deposited on 1 g of SBA-15. A Mo loading of ~7 wt% in the resulting $H_4[PVMo_{11}O_{40}]$-SBA-15 catalyst was determined by ICP-OES analysis (Jobin Yvon JY 38 Plus). Commercial α-MoO_3 (Aldrich) and hexagonal MoO_3 were used as reference materials [32,33]. Phase purity and structure of the reference oxides were confirmed by XRD.

2.2. Powder X-ray diffraction (XRD)

XRD measurements were conducted on an X'Pert PRO MPD diffractometer (Panalytical, θ–θ geometry), using Cu K alpha radiation and a solid-state multi-channel PIXcel detector. Wide-angle scans (5–90° 2θ, variable slits) were collected in reflection mode using a silicon sample holder. Small-angle scans (0.4–6.0° 2θ, fixed slits) were collected in transmission mode with the sample spread between two layers of Kapton foil and in reflection mode for comparison.

2.3. Physisorption measurements

Nitrogen physisorption isotherms were measured at 77 K on a BEL Mini II volumetric sorption analyzer (BEL Japan, Inc.). The $H_4[PVMo_{11}O_{40}]$-SBA-15 sample was outgassed under vacuum for about 18 h at 553 K before starting the measurement. After outgassing, the sample color had turned from yellow to dark gray. This pretreatment procedure was chosen to approach catalytic reaction conditions. Data processing was done using the BELMaster V.5.2.3.0 software package. The specific surface area was calculated using the standard Brunauer–Emmett–Teller (BET) method in the relative pressure range of 0.05–0.20 with a nitrogen area of 0.162 nm^2. The adsorption branch of the isotherm was used to calculate pore size distribution and cumulative pore area according to the method of Barrett, Joyner, and Halenda (BJH) [34].

2.4. X-ray absorption spectroscopy (XAS)

Ex situ fluorescence yield XAS experiments were performed at the V K edge (5.6 keV) at beamline XAS at *ANKA*, Karlsruhe, using a Si(1 1 1) double crystal monochromator and a Ge 13 element FY detector. Ex situ transmission XAS experiments at the Mo K edge (19.999 keV) were also performed at the XAS beamline at *ANKA* using a Si(3 1 1) monochromator. In situ transmission XAS experiments were performed at the Mo K edge at beamline X at the *Hamburg Synchrotron Radiation Laboratory*, HASYLAB, using a Si(1 1 1) double crystal monochromator (measuring time ~4 min/scan). The Si(1 1 1) monochromator resulted in an improved signal-to-noise ratio in the EXAFS region on expense of resolution in the XANES region. The in situ experiments were conducted in a flow reactor at atmospheric pressure in flowing reactants (5 vol% propene in He, 5 vol% oxygen in He, total flow ~30 ml/min, temperature range from 300 K to 773 K, heating rate 4 K/min). The gas phase composition at the cell outlet was continuously monitored using a non-calibrated mass spectrometer in a multiple ion detection mode (Omnistar from Pfeiffer). The mass spectrometer was used for its suitable time resolution. Because a channeltron was employed as detector, long-time stable calibration and quantification were not feasible. Moreover, a quantitative comparison

with more active or industrial catalysts was not intended. Conversion of propene was estimated from the propene ion current (m/e 42) before and during reaction to be less than 10% at 673 K. $H_3[PMo_{12}O_{40}]\cdot nH_2O$ and $H_4[PVMo_{11}O_{40}]\cdot 13H_2O$ were mixed with boron nitride (~7 mg each with 30 mg BN) while supported HPOM-SBA-15 materials (~50 mg) were used as-is. Powders were pressed with a force of 1 ton into a 5 mm in diameter pellet resulting in an edge jump at the Mo K edge of $\Delta\mu_x \sim 1$.

X-ray absorption fine structure (XAFS) analysis was performed using the software package WinXAS v3.2 [35]. Background subtraction and normalization were carried out by fitting linear polynomials to the pre-edge and 3rd degree polynomials to the post-edge region of an absorption spectrum, respectively. The extended X-ray absorption fine structure (EXAFS) $\chi(k)$ was extracted by using cubic splines to obtain a smooth atomic background $\mu_0(k)$. The FT($\chi(k) * k^3$), often referred to as pseudo radial distribution function, was calculated by Fourier transforming the k^3-weighted experimental $\chi(k)$ function, multiplied by a Bessel window, into the R space. EXAFS data analysis was performed using theoretical backscattering phases and amplitudes calculated with the ab-initio multiple-scattering code FEFF7 [36]. Structural data employed in the analyses were taken from the Inorganic Crystal Structure Database (ICSD). Single scattering and multiple scattering paths in the $H_3[PMo_{12}O_{40}]$ Keggin model structure (ICSD 209 [37,16]) were calculated up to 6.0 Å with a lower limit of 4.0% in amplitude with respect to the strongest backscattering path. EXAFS refinements were performed in R space simultaneously to magnitude and imaginary part of a Fourier transformed k^3-weighted and k^1-weighted experimental $\chi(k)$ using the standard EXAFS formula [38]. This procedure strongly reduces the correlation between the various XAFS fitting parameters. Structural parameters allowed to vary in the refinement were (i) disorder parameter σ^2 of selected single-scattering paths assuming a symmetrical pair-distribution function and (ii) distances of selected single-scattering paths. In the XAFS analysis, it is assumed that the Mo centers are largely situated in intact Keggin ions in the as-prepared materials. Thus, the number of nearest neighbors around the Mo centers is independent of the tertiary structure of the HPOM, i.e. the arrangement of the Keggin ions either in the solid or on a high surface area support material. Therefore, coordination numbers (N) as well as E_0 shifts and amplitude reduction factor S_0^2 were kept invariant in the final fitting procedures. Correlations of specific parameters to reduce the number of free running parameters and to improve the stability of the refinement are described in the following paragraphs.

The statistical significance of the fitting procedure employed was carefully evaluated in three steps [39]. The procedures used correspond to recommendations of the *International X-ray Absorption Society* on criteria and error reports [40]. First, the number of independent parameters (N_{ind}) was calculated according to the Nyquist theorem $N_{ind} = 2/\pi * \Delta R * \Delta k + 2$. In all cases, the number of free running parameters in the refinements was well below N_{ind}. Second, confidence limits were calculated for each individual parameter. In the corresponding procedure, one parameter was successively varied by a certain percentage (i.e. 0.05% for R and 5% for σ^2) and the refinement was restarted with this parameter kept invariant. The parameter was repeatedly increased or decreased until the fit residual exceed the original fit residual by more than 5%. Eventually, the confidence limit of the parameter was obtained from linear interpolation between the last and second last increment for an increase in fit residual of 5%. This procedure was consecutively performed for each fitting parameter. Third, a so-called F test was performed to assess the significance of the effect of additional fitting parameters on the fit residual [41]. Fit parameters employed exhibited F values below 0.2 and are statistically significant.

3. Results and discussion

3.1. Long-range order structural characterization of $PVMo_{11}$-SBA-15

$H_4[PVMo_{11}O_{40}]$ Keggin ions supported on SBA-15 (denoted as $PVMo_{11}$-SBA-15) were prepared by incipient wetness of silica SBA-15 with suitable precursor solutions. Structure and properties of the resulting material were studied ex situ by XRD and nitrogen physisorption measurements and in situ by combined X-ray absorption spectroscopy (XAS) and mass spectrometry under various reaction conditions. The characteristic structure of $PVMo_{11}$-SBA-15 and its structural evolution under reactive gas atmosphere are compared to that of bulk $H_4[PVMo_{11}O_{40}]\cdot 13H_2O$ (denoted as $PVMo_{11}$) in the following. The results presented focus on the structural characteristics of $PVMo_{11}$-SBA-15. Very similar structural results were obtained for PMo_{12}-SBA-15, and $PVMo_{11}$ and PMo_{12} supported on various oxide support material (i.e. Al_2O_3, ZrO_2, SiO_2). Effects of support interactions and preparation conditions on structural and catalytic properties of these materials will be the subject of future work.

Small-angle and wide-angle X-ray diffraction patterns of $PVMo_{11}$-SBA-15 are presented in Fig. 1. Compared to the XRD pattern of $H_4[PVMo_{11}O_{40}]\cdot 13H_2O$, it can be seen that long-range ordered HPOM species were not detectable in the $PVMo_{11}$-SBA-15 material. At small diffraction angles, $PVMo_{11}$-SBA-15 exhibited the characteristic pattern of nanostructured silica SBA-15 [24]. Evaluation of the (1 0 0) peak position of SBA-15 (Fig. 1) afforded a lattice constant of the hexagonal unit cell of a = 11.9 nm.

BET surface areas were calculated from physisorption data of SBA-15 and $PVMo_{11}$-SBA-15. While the SBA-15 material used exhibited a surface area of 767 $m^2\,g^{-1}$, $PVMo_{11}$-SBA-15 exhibited a surface area of 482 $m^2\,g^{-1}$. The physisorption isotherm of $PVMo_{11}$-SBA-15 is depicted in Fig. 2. The isotherm exhibits a sharp step in the adsorption branch (Type IV), corresponding to the filling of well-defined mesopores. The inset of Fig. 2 shows the pore size distribution of $PVMo_{11}$-SBA-15 and SBA-15. Both exhibited narrow distributions with a peak at a pore radius of 4.0 nm. Given a pore diameter of 8 nm and an XRD lattice constant of 11.9 nm, the wall thickness of the SBA-15 material used amounted to 3.9 nm. The BJH cumulative pore area down to 1.2 nm pore radius amounted to 339 $m^2\,g^{-1}$. In total, similar adsorption isotherms and pore size distributions of $PVMo_{11}$-SBA-15 and SBA-15 confirm the conserved SBA-15 structure after deposition and thermal treatment of the HPOM. Eventually, the BJH cumulative pore area of 339 $m^2\,g^{-1}$

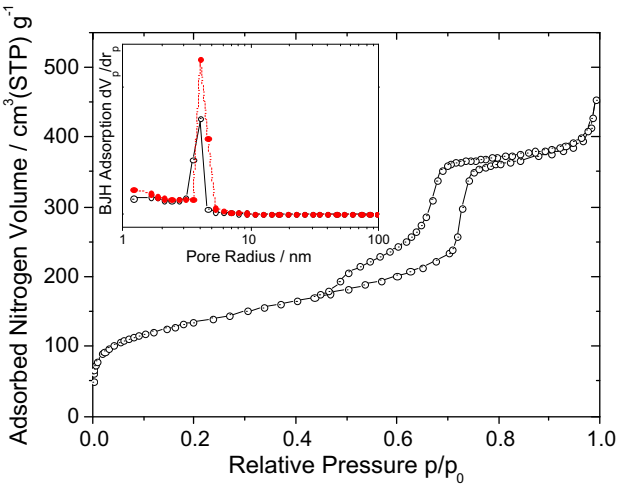

Fig. 2. Nitrogen physisorption isotherms of $PVMo_{11}$-SBA-15 and pore size distribution of silica SBA-15 (filled circles) and $PVMo_{11}$-SBA-15 (open circles) (inset).

was used to estimate the dispersion of Keggin ions on the accessible SBA-15 surface. Given a Mo loading of ~7 wt% in the $PVMo_{11}$-SBA-15 catalyst, a surface coverage of about one Keggin ion per 10 nm^2 was obtained. Assuming a Keggin ion diameter of about 1 nm, this indicated sufficient dispersion of Keggin ions on the SBA-15 surface and negligible tendency to form extended tertiary HPOM structures.

3.2. Short-range order structural characterization of $PVMo_{11}$-SBA-15

Fig. 3 shows the XAS $\chi(k)$ data of $PVMo_{11}$-SBA-15, bulk $PVMo_{11}$, and activated $PVMo_{11}$-SBA-15. The good signal-to-noise ratio of the XAS data in the k range from 2 to 13 $Å^{-1}$ permitted the detailed XAFS analysis described later. The Mo K edge Fourier transformed XAFS $\chi(k)$ functions ($FT(\chi(k)*k^3)$) of bulk and supported HPOM with and without vanadium are compared in Fig. 4. The very similar shape of the magnitude of the ($FT(\chi(k)*k^3)$) indicates a similar local structure around the Mo centers in the four materials. It appears that while introducing V in the HPOM Keggin structure resulted in a slight decrease in amplitude, supporting the HPOM on SiO_2 resulted in an increased amplitude of the corresponding $FT(\chi(k)*k^3)$.

In the following, we focused our investigations on the vanadium containing HPOM as model system for mixed oxide catalysts. The Mo K near-edge spectra (XANES) of $PVMo_{11}$-SBA-15 and activated $PVMo_{11}$-SBA-15 are depicted in Fig. 5. The Mo K edge XANES of as-prepared $PVMo_{11}$-SBA-15 is very similar to previously reported XANES spectra of bulk PMo_{12} and $PVMo_{11}$ [16–18]. Analysis of the Mo K edge position yielded an average valence of ~6. Because of the inferior resolution of the Si(1 1 1) monochromator used for XAS studies under reaction conditions, no detailed XANES analysis with respect to principal components or molybdenum valence was attempted. Fig. 5 also shows the V K edge XANES spectra of $PVMo_{11}$-SBA-15 and bulk $PVMo_{11}$. Compared to vanadium oxide reference compounds, the pre-edge peak at the V K edge indicates an average valence between 4 and 5, as previously reported for bulk $PVMo_{11}$ [17,18]. The pre-edge peak and, thus, the electronic structure appear to be little effected by support interaction. Conversely, the amplitude of the post-edge XANES features of $PVMo_{11}$-SBA-15 is significantly reduced compared to that of bulk $PVMo_{11}$. This reduced amplitude may be indicative of a reduced medium range order and the dispersion of the Keggin ions on the silica support. Therefore, this effect appears to be more pronounced in the XANES region than in EXAFS region (Fig. 6).

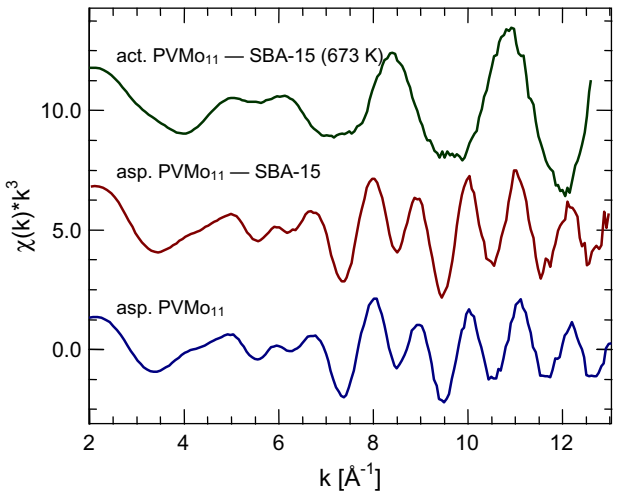

Fig. 3. Mo K edge XAFS $\chi(k)$ of $H_4[PVMo_{11}O_{40}]$, as-prepared $PVMo_{11}$-SBA-15, and activated $PVMo_{11}$-SBA-15 after thermal treatment in propene and oxygen at 673 K.

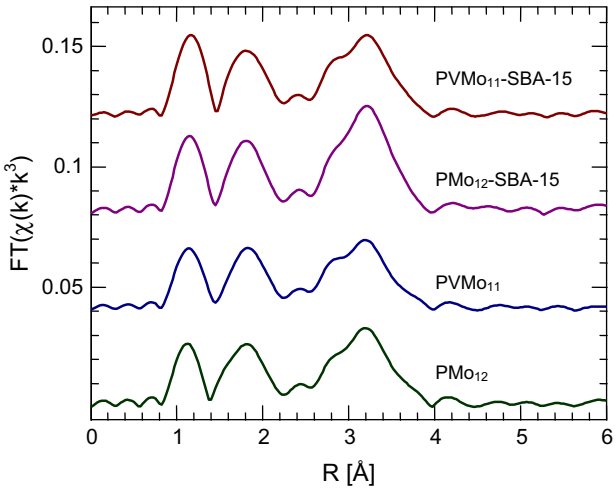

Fig. 4. Mo K edge $FT(\chi(k)*k^3)$ of reference HPOM materials ($H_3[PMo_{12}O_{40}]$ and $H_4[PVMo_{11}O_{40}]$) and HPOM supported on SBA-15 (PMo_{12}-SBA-15 and $PVMo_{11}$-SBA-15).

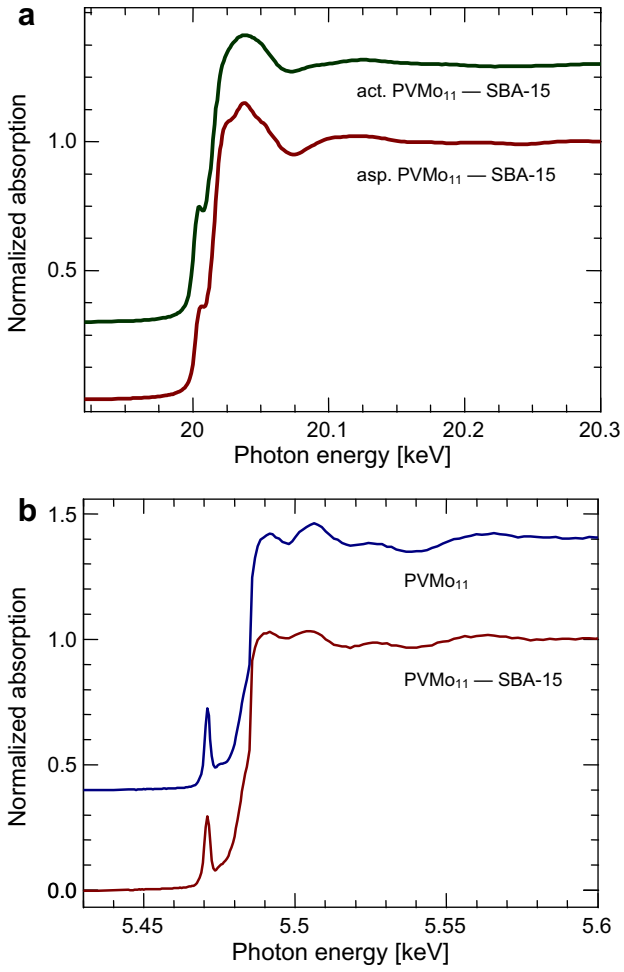

Fig. 5. (a) Mo K edge XANES spectra of as-prepared $PVM._{11}$-SBA-15, and activated $PVMo_{11}$-SBA-15 after thermal treatment in propene and oxygen at 673 K and (b) V K edge XANES spectra of $H_4[PVMo_{11}O_{40}]$ and as-prepared $PVMo_{11}$-SBA-15.

Fig. 6 shows the Mo K edge and V K edge $FT(\chi(k)*k^3)$ (magnitude and imaginary part) of $PVMo_{11}$-SBA-15 and bulk $PVMo_{11}$. The Fourier transformed XAFS $\chi(k)*k^3$ are not phase-shift corrected. Thus, the distances in the magnitude of the $FT(\chi(k)*k^3)$ are shifted

by ~0.4 Å to lower values compared to the crystallographic distances. Over the local structural range accessible to XAFS spectroscopy (~6 Å), the FT($\chi(k)*k^3$) of $PVMo_{11}$-SBA-15 strongly resembles that of bulk $PVMo_{11}$. This holds for the local coordination of both V and Mo centers in the respective Keggin ions (Fig. 6). The Mo K edge and V K edge FT($\chi(k)*k^3$) of $PVMo_{11}$-SBA-15 are compared in Fig. 7. Fourier transformation of experimental $\chi(k)$ data was performed in the same spectral range. Similar amplitudes and imaginary parts at distances above 1.5 Å (not phase-shift corrected) indicate a similar local structure around the Mo and V centers. This further corroborates the assumption of V being located on Mo sites in the supported Keggin ions. The main differences between the two FT($\chi(k)*k^3$) is visible in the amplitude of the first M–O coordination sphere (Fig. 7). Assuming the same number of nearest oxygen neighbors around both metal centers, the increased amplitude of the V K edge FT($\chi(k)*k^3$) is indicative of narrower distance distribution and similar V–O distances in the 2 Å range. Apparently, the Keggin ion primary and secondary structure (i.e. characteristic MoO_6 units and arrangement of these units, Fig. 8) is preserved in $PVMo_{11}$ supported on SBA-15. In contrast, the tertiary structure (i.e. arrangement of Keggin ions) of $H_4[PVMo_{11}O_{40}]\cdot 13H_2O$ is not observed (Fig. 1). This further suggests the presence of supported $PVMo_{11}$ Keggin ions on silica SBA-15 which will also be corroborated by chemical reactivity studies.

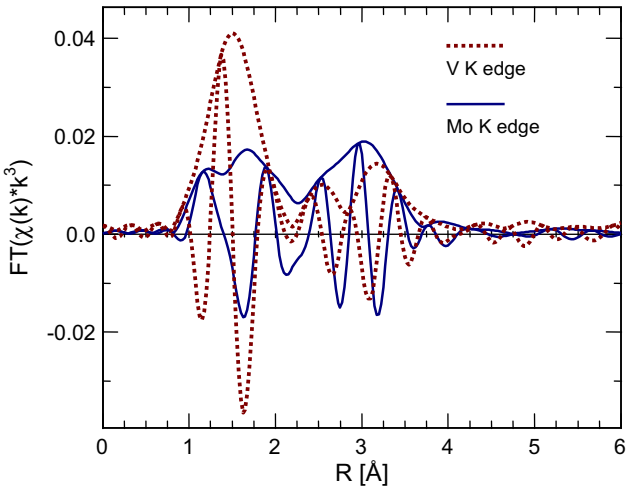

Fig. 7. Direct comparison of Mo K edge (solid) and V K edge (dotted) FT($\chi(k)*k^3$) of as-prepared $PVMo_{11}$-SBA-15 in the same spectral k range (1.5–11.0 $Å^{-1}$).

Based on the similar FT($\chi(k)*k^3$) of bulk $PVMo_{11}$ and $PVMo_{11}$-SBA-15, the local structure around Mo centers in bulk $PVMo_{11}$ according to crystallographic data was used as model system for a detailed EXAFS analysis. Theoretical and experimental Mo K edge

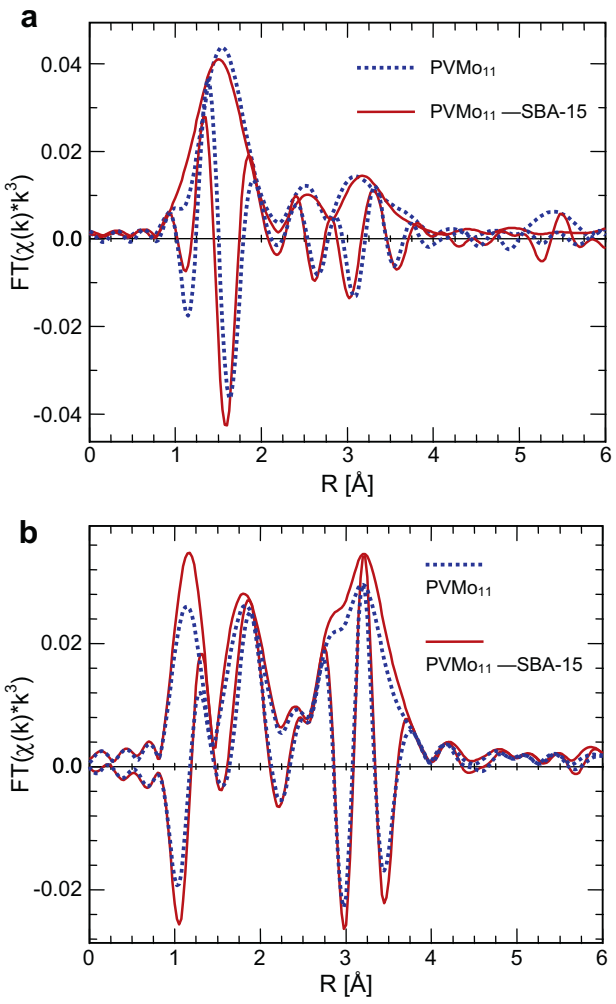

Fig. 6. (a) Mo K edge FT($\chi(k)*k^3$) and (b) V K edge XAFS FT($\chi(k)*k^3$) of $H_4[PVMo_{11}O_{40}]$ and as-prepared $PVMo_{11}$-SBA-15.

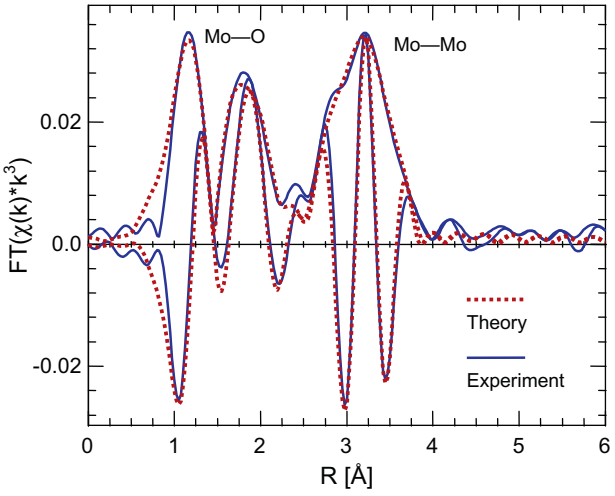

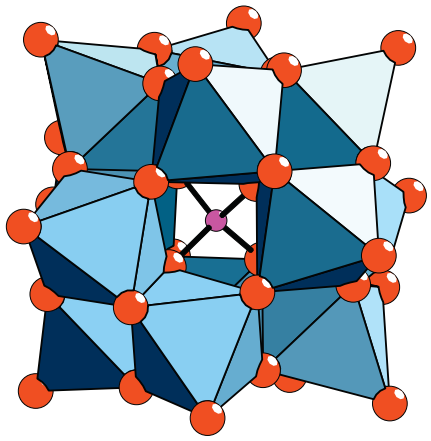

Fig. 8. Theoretical (dotted) and experimental (solid) Mo K edge FT($\chi(k)*k^3$) of $PVMo_{11}$-SBA-15 together with a schematic representation of the Keggin structure. Mo–O corresponds to distances in the first coordination sphere, while Mo–Mo corresponds to two distances between edge and corner-sharing MoO_6 units in the Keggin structure (Table 1).

FT($\chi(k)*k^3$) of $PVMo_{11}$-SBA-15 are shown in Fig. 8 together with a schematic representation of the Keggin structure. The good agreement between theory and experiment for both $PVMo_{11}$-SBA-15 and bulk $PVMo_{11}$ corroborates the conclusion that the majority of Mo centers in $PVMo_{11}$-SBA-15 is situated in Keggin type HPOM supported on SBA-15. Structural parameters obtained from the XAFS refinement are given in Table 1. While the Mo–O and Mo–Mo distances are nearly identical in $PVMo_{11}$-SBA-15 and bulk $PVMo_{11}$, the σ^2 parameters are slightly decreased in the $PVMo_{11}$-SBA-15 material. The resulting decreased damping of the EXAFS function accounts for the slightly increased amplitude of $PVMo_{11}$-SBA-15 compared to bulk $PVMo_{11}$. Compared to the theoretical model system, a pronounced splitting of the first Mo–O coordination sphere can be seen. Apparently, a broadened distance distribution is required to simulate the characteristic FT($\chi(k)*k^3$) of both $PVMo_{11}$-SBA-15 and bulk $PVMo_{11}$. This was also observed in previous studies [16,17].

Theoretical and experimental V K edge FT($\chi(k)*k^3$) of $PVMo_{11}$-SBA-15 are depicted in Fig. 9. Similar to the Mo K edge data, the good agreement between theory and experiment corroborates the conclusion that the majority of V centers in both $PVMo_{11}$ and $PVMo_{11}$-SBA-15 is located on Mo sites in Keggin type HPOM. Structural parameters obtained from a XAFS refinement are given in Table 2. In contrast to the local structure around the Mo centers, the V centers in the Keggin ion exhibited a narrowed distance distribution with four nearly identical V–O distances in the equatorial plane of the VO_6 unit. The necessity to reduce the number of independent V–O distances also resulted from evaluating the statistical *F* parameters and the corresponding confidence limits. The four V–O distances in the first coordination shell dominate the overall single-peak shape of that region in the FT($\chi(k)*k^3$) (Fig. 9) compared to the double peak feature in the Mo K edge EXAFS (Fig. 8). The V–O distance distribution in the FT($\chi(k)*k^3$) of $PVMo_{11}$-SBA-15 appears to be more similar to the theoretical reference used than the local structure around the Mo centers. In total, the structural characterization of the as-prepared materials clearly showed that both V free PMo_{12} and V containing $PVMo_{11}$ Keggin ions can be readily supported on silica SBA-15. The preparation conditions required are similar to those regularly used for the respective unsupported materials. Moreover, local structure around the metal centers and their electronic structure are similar in both supported and unsupported PMo_{12} and $PVMo_{11}$ Keggin ions.

3.3. Treatment of $PVMo_{11}$-SBA-15 under reducing conditions

The effect of support interactions on the chemical reactivity of $PVMo_{11}$-SBA-15 compared to bulk $PVMo_{11}$ was studied by in situ XAS under reducing and catalytic reaction conditions. Evolution of Mo K edge FT($\chi(k)*k^3$) of $PVMo_{11}$-SBA-15 and bulk $PVMo_{11}$ during temperature-programmed treatment in propene is depicted in Fig. 10. The corresponding XANES data exhibited only very minor changes as a function of temperature and, thus, are omitted for brevity. In contrast to regular MoO_3 and similar to stabilized hexagonal MoO_3 on SBA-15 [11], no full reduction to MoO_2 was observed during treatment of $PVMo_{11}$-SBA-15 in propene. The structural evolution of bulk $PVMo_{11}$ in propene proceeded according to previous reports and also showed no reduction to MoO_2. [17,18] As shown previously, reductive treatment of bulk $PVMo_{11}$ affords partial decomposition of the Keggin ions by migration of Mo centers on extra-Keggin sites and formation of lacunary Keggin ions. However, the structural changes observed in $PVMo_{11}$-SBA-15 during treatment in propene were distinctly different from those of bulk $PVMo_{11}$. Contribution of higher Mo–Mo shells to the FT($\chi(k)*k^3$) of activated $PVMo_{11}$-SBA-15 was largely diminished after reductive treatment. In contrast to the treatment of bulk $PVMo_{11}$, this thermal behavior is indicative of a higher degree of dispersion of the corresponding Mo oxide species on silica SBA-15. Moreover, the increasing amplitude of the first Mo–O coordination sphere during treatment of $PVMo_{11}$-SBA-15 indicates a more regular coordination and a reduced number of different Mo–O distances in the activated species. Apparently, the silica support in

Table 1
Type and number (*N*) of atoms at distance *R* from the Mo atoms in a [$PMo_{12}O_{40}$] Keggin model system compared to experimental distances and disorder parameters (σ^2). Experimental parameters were obtained from a refinement of the Keggin model structure (ICSD 209) to the experimental Mo K edge XAFS $\chi(k)$ of $PVMo_{11}$ and $PVMo_{11}$-SBA-15 (Fig. 8) (*k* range from 3.4 to 13.3 Å^{-1}, R range from 0.8 to 4.0 Å, E_0 = 8.0 eV, residual ~9.0, N_{ind} = 22, N_{free} = 12). Confidence limits in distances and σ^2 parameters amounted to about 0.01 Å (0.03 Å for Mo–P) and 0.0002 Å^2 for Mo–Mo and 0.0007 Å^2 for Mo–O, respectively. Subscript C indicates parameters that were correlated in the refinement.

Type	Keggin model		$PVMo_{11}$		$PVMo_{11}$-SBA-15	
	N	*R* (Å)	*R* (Å)	σ^2 (Å^2)	*R* (Å)	σ^2 (Å^2)
Mo–O	1	1.70	1.65	0.0049	1.65	0.0031
Mo–O	2	1.91	1.77	0.0068_C	1.78	0.0052_C
Mo–O	2	1.92	1.95	0.0068_C	1.95	0.0052_C
Mo–O	1	2.43	2.39	0.0016	2.39	0.0010
Mo–Mo	2	3.42	3.41	0.0079_C	3.42	0.0070_C
Mo–P	1	3.56	3.47	0.0034	3.48	0.0028
Mo–Mo	2	3.70	3.71	0.0079_C	3.72	0.0070_C

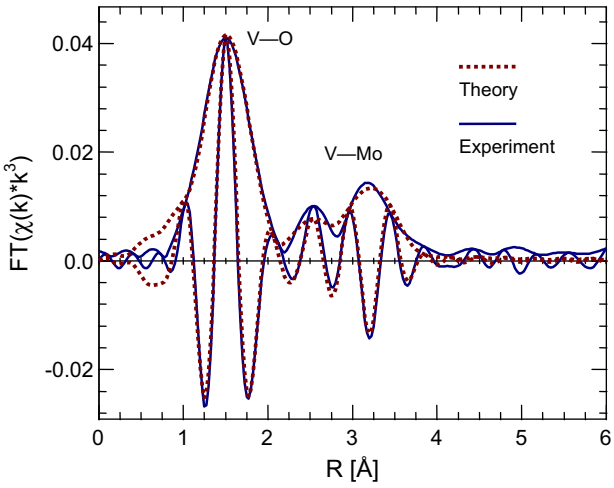

Fig. 9. Theoretical (dotted) and experimental (solid) V K edge FT($\chi(k)*k^3$) of $PVMo_{11}$-SBA-15. V–O corresponds to distances in the first coordination sphere, while Mo–V corresponds to two distances between edge and corner-sharing VO_6–MoO_6 units in the Keggin structure (Table 2).

Table 2
Type and number (*N*) of atoms at distance *R* from the V atoms in a [$PVMo_{11}O_{40}$] Keggin model system compared to experimental distances and XAFS disorder parameters (σ^2). Experimental parameters were obtained from a refinement of the Keggin model structure (ICSD 209) to the experimental V K edge XAFS $\chi(k)$ of $PVMo_{11}$ and $PVMo_{11}$-SBA-15 (Fig. 9) (*k* range from 1.5 to 11.0 Å^{-1}, *R* range from 0.8 to 4.0 Å, E_0 = −9.0 eV, residual ~9.5, N_{ind} = 21, N_{free} = 11). Confidence limits in distances and σ^2 parameters amounted to about 0.02 Å and 0.0002 Å^2 for V–Mo and 0.0007 Å^2 for V–O, respectively. Subscript C indicates parameters that were correlated in the refinement.

Type	Keggin model		$PVMo_{11}$		$PVMo_{11}$-SBA-15	
	N	*R* (Å)	*R* (Å)	σ^2 (Å^2)	*R* (Å)	σ^2 (Å^2)
V–O	1	1.70	1.64	0.0035	1.63	0.0021
V–O	2	1.91	1.97_C	0.0117_C	1.92_C	0.0112_C
V–O	2	1.92	1.97_C	0.0117_C	1.92_C	0.0112_C
V–O	1	2.43	2.37	0.0057	2.39	0.0032
V–Mo	2	3.42	3.34	0.0087_C	3.35	0.0087_C
V–P	1	3.56	3.47	0.0002	0.0	0.0003
V–Mo	2	3.70	3.68	0.0087_C	3.71	0.0087_C

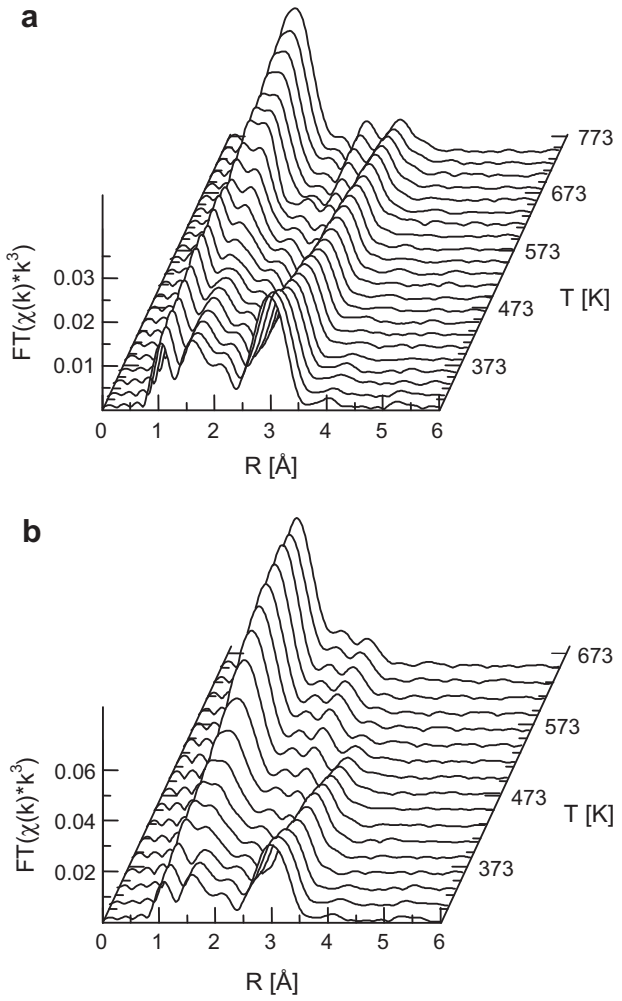

Fig. 10. Evolution of Mo K edge FT($\chi(k) * k^3$) of (a) $H_4[PVMo_{11}O_{40}]$ and (b) as-prepared $PVMo_{11}$-SBA-15 during temperature-programmed treatment in propene (4 K/min, 5% propene in He).

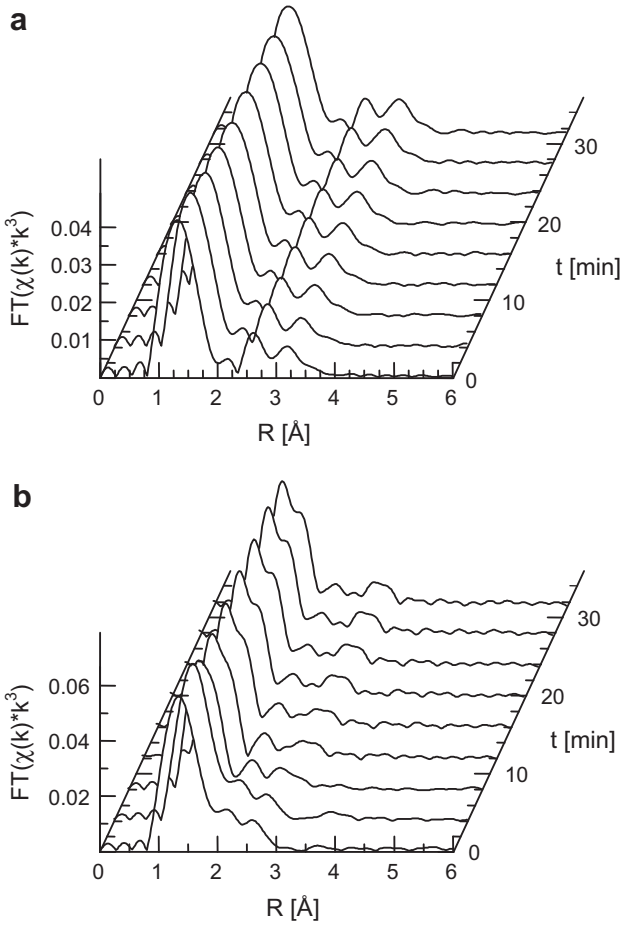

Fig. 11. Evolution of Mo K edge FT($\chi(k) * k^3$) of (a) $H_4[PVMo_{11}O_{40}]$ and (b) $PVMo_{11}$-SBA-15 during isothermal switching after the first spectrum from propene (5% in He) to propene and oxygen atmosphere (5% propene and 5% oxygen in He) at 623 K after temperature-programmed activation in propene (Fig. 10).

$PVMo_{11}$-SBA-15 exerted a pronounced effect on the reactivity of $PVMo_{11}$-SBA-15 compared to bulk $PVMo_{11}$. Formation of lacunary Keggin ions as in bulk $PVMo_{11}$ was not observed. Conversely, thermal treatment of $PVMo_{11}$-SBA-15 resulted in formation of dispersed Mo oxide species on the silica support. The characteristic differences in reactivity of $PVMo_{11}$-SBA-15 compared to bulk $PVMo_{11}$ further corroborated the presence of dispersed $PVMo_{11}$ Keggin ions on the silica surface in the as-prepared $PVMo_{11}$-SBA-15 material.

After reductive treatment of $PVMo_{11}$ and $PVMo_{11}$-SBA-15 in propene (Fig. 10), the gas phase composition was rapidly changed to oxidizing conditions (5% propene and 5% oxygen in He) at 673 K. The evolution of the corresponding FT($\chi(k) * k^3$) is depicted in Fig. 11. The FT($\chi(k) * k^3$) of activated bulk $PVMo_{11}$ remained largely invariant during switching to catalytic reaction conditions as has been reported earlier [17,18]. Apparently, lacunary Keggin ions in activated bulk $PVMo_{11}$ constitute the Mo oxide phase present under catalytic reaction conditions. Conversely, the FT($\chi(k) * k^3$) of activated $PVMo_{11}$-SBA-15 showed characteristic changes in the first Mo–O coordination sphere and at higher Mo–Mo distances upon switching to oxidizing conditions. This behavior can again be attributed to the effect of the silica support interaction on the properties of the Mo oxide species in activated $PVMo_{11}$-SBA-15. Furthermore, higher Mo–Mo interactions appeared to develop during oxidative treatment of previously activated $PVMo_{11}$-SBA-15. Apparently, the dispersed Mo oxide species in activated $PVMo_{11}$-SBA-15 formed dimers or chains under catalytic reaction conditions at elevated temperatures.

3.4. Treatment of $PVMo_{11}$ -SBA-15 under catalytic conditions

After having studied the structural changes of $PVMo_{11}$-SBA-15 separately under reducing and oxidizing conditions (Figs. 10 and 11), in situ XAS studies were performed during thermal treatment of $PVMo_{11}$-SBA-15 under catalytic reaction conditions. Evolution of Mo K edge FT($\chi(k) * k^3$) of $PVMo_{11}$-SBA-15 during treatment in propene and oxygen in the temperature range from 300 to 673 K is depicted in Fig. 12. Again, the corresponding XANES data exhibited only very minor changes as a function of temperature and are omitted for brevity. The characteristic changes in FT($\chi(k) * k^3$) in Fig. 12 indicate a multiple-step process during evolution of the local structure of $PVMo_{11}$-SBA-15 under reaction conditions. At 673 K, the resulting FT($\chi(k) * k^3$) strongly resembled that obtained after consecutive treatment under reducing (Fig. 10) and oxidizing (Fig. 11) reaction conditions. In total the evolution of FT($\chi(k) * k^3$) of $PVMo_{11}$-SBA-15 depicted in Fig. 12 appears to be composed of the two series of spectra depicted in Figs. 10 and 11. Accordingly, the structural evolution of $PVMo_{11}$-SBA-15 in propene and oxygen in the temperature range from 300 K to 523 K corresponded to that observed during treatment in propene (Fig. 10). At 523 K, the amplitude of higher Mo–Mo shells was largely diminished and the corresponding FT($\chi(k) * k^3$) indicated a high dispersion of Mo

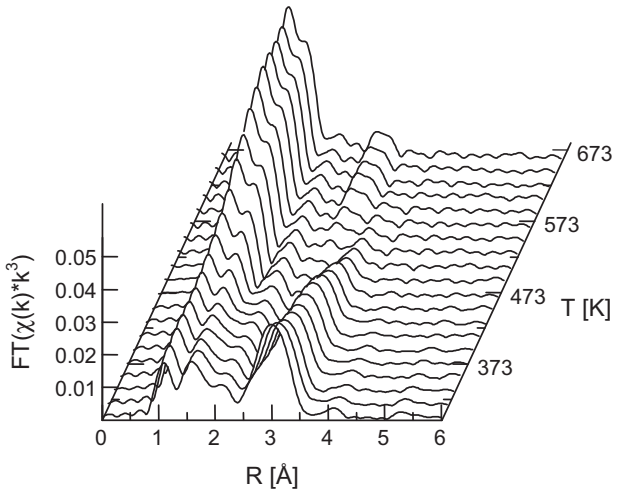

Fig. 12. Evolution of Mo K edge FT($\chi(k) * k^3$) of as-prepared $PVMo_{11}$-SBA-15 during temperature-programmed treatment in propene and oxygen (4 K/min, 5% propene and 5% oxygen in He).

oxide species on silica SBA-15. In the temperature range from 523 K to 673 K, the structural evolution of $PVMo_{11}$-SBA-15 in propene and oxygen was very similar to that depicted in Fig. 11 for the oxidative treatment of formerly activated $PVMo_{11}$-SBA-15. The characteristic appearance of higher Mo–Mo distances in Fig. 12 above 573 K indicates the formation of dimeric or polymeric Mo_xO_y species under catalytic reaction conditions. Apparently, the characteristic decomposition of the Keggin HPOM in the temperature range from 300 K to 573 K proceeded irrespectively of the gas phase composition. A certain structure directing behavior of the silica support and the stability of the resulting Mo oxide species may be responsible for the transformation of the supported Keggin ions to dispersed Mo oxide species. Conversely, the formation of polymeric activated Mo species required the presence of gas phase oxygen.

Quantitative catalysis measurements performed as described in Ref. [42] yielded a propene conversion of ~8% at 673 K. Concentrations of major oxidation products measured in the in situ cell exhaust amounted to 2500 ppm CO_2, 620 ppm acrolein, and 32 ppm acrylic acid. Similar to bulk $PVMo_{11}$, α-MoO_3, and MoO_x-SBA-15 $PVMo_{11}$-SBA-15 showed the typical onset of catalytic activity at about 600 K [17,11]. The onset temperature of 600 K largely coincides with the onset of lattice oxygen mobility and availability of lattice oxygen to the gaseous reactants [43,44]. However, α-MoO_3 does not selectively oxidize propene directly to acrylic acid. Hence, the onset of propene oxidation at ~600 K on activated $PVMo_{11}$-SBA-15 and the evolution of selective and total oxidation products were found to be similar to that observed during thermal treatment and catalytic studies on hexagonal MoO_3 species supported on SBA-15 [11].

3.5. Local structure of activated $PVMo_{11}$-SBA-15 under catalytic conditions

Mo K edge XANES spectra of as-prepared and activated $PVMo_{11}$-SBA-15 are depicted in Fig. 5. The nearly featureless XANES region of activated $PVMo_{11}$-SBA-15 compared to that of the as-prepared material or reference α-MoO_3 is indicative of dispersed Mo species supported on SBA-15. A slight increase in the pre-edge feature of the Mo K edge XANES of activated $PVMo_{11}$-SBA-15 is visible compared to the spectrum of as-prepared $PVMo_{11}$-SBA-15. The pre-edge peak in the Mo K edge XANES of $PVMo_{11}$ is attributed to the distorted MoO_6 building unit of the Keggin ion.

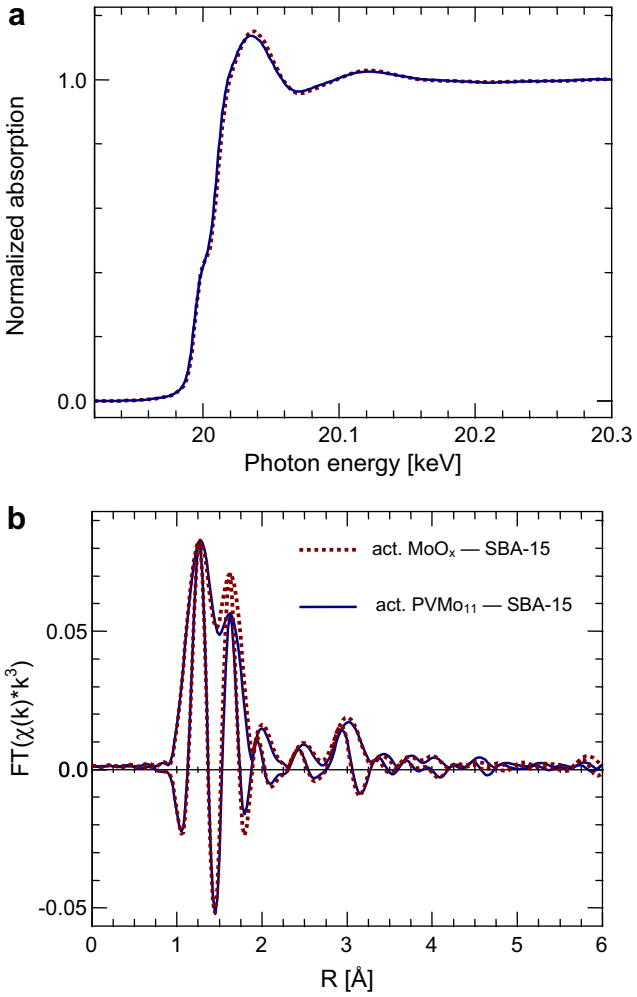

Fig. 13. (a) Mo K edge XANES spectra and (b) FT($\chi(k) * k^3$) of activated $PVMo_{11}$-SBA-15 (solid) and activated MoO_x-SBA-15 (dashed) after thermal treatment in oxygen at 673 K.

Conversely, the further increased pre-edge peak in the spectrum of activated $PVMo_{11}$-SBA-15 indicates the presence of tetrahedrally coordinated Mo centers in the MoO_x species in activated $PVMo_{11}$-SBA-15. Comparison with references afforded about 50% of tetrahedrally coordinated MoO_x species supported on SBA-15. Due to the lack of reference spectra measured with the same resolution, no further quantitative edge analysis could be conducted. The same holds for the in situ XAFS data measured under reaction conditions.

While seeking a suitable model system to simulate the experimental FT($\chi(k) * k^3$) of activated $PVMo_{11}$-SBA-15 it became apparent that two Mo–Mo distances like in the Keggin $PVMo_{11}$ structure were not sufficient. In spite of the reduced amplitude at higher shells, three Mo–Mo distances were required to account for the particular shape of the amplitude and imaginary part of the FT($\chi(k) * k^3$) of activated $PVMo_{11}$-SBA-15 in the range between 2.5 and 3.5 Å (Fig. 13). Therefore, hexagonal MoO_3 was used as model system. Theoretical XAFS phases and amplitudes were calculated for Mo–O and Mo–Mo distances in hex-MoO_3 and used for EXAFS refinement. Theoretical and experimental Mo K edge FT($\chi(k) * k^3$) of activated $PVMo_{11}$-SBA-15 are shown in Fig. 14. Structural parameters obtained from the XAFS refinement are given in Table 3. The reduced FT($\chi(k) * k^3$) amplitude at higher shells in Fig. 14 indicates a strong disorder or small extension of the MoO_x species supported on SBA-15. However, the fitting procedure

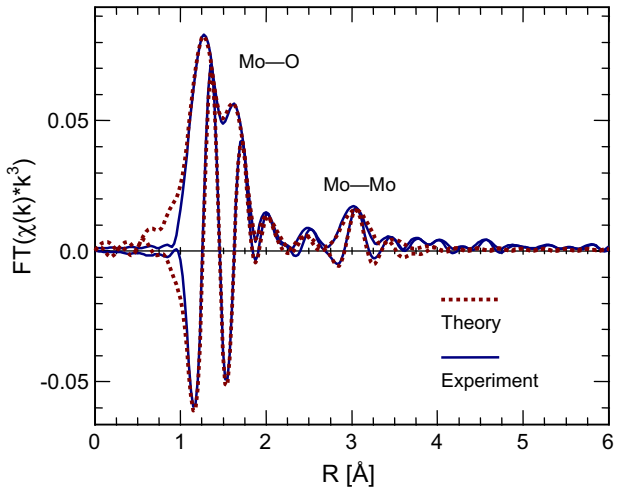

Fig. 14. Theoretical (dotted) and experimental (solid) Mo K edge FT($\chi(k) * k^3$) of activated $PVMo_{11}$-SBA-15. Structural parameters are given in Table 3.

Table 3
Type, number (N), and XAFS disorder parameters (σ^2) of atoms at distance R from the Mo atoms in MoO_x species in activated $PVMo_{11}$-SBA-15. Experimental parameters were obtained from a refinement of a MoO_3 model structure to the experimental Mo K edge XAFS $\chi(k)$ of activated $PVMo_{11}$-SBA-15 (Fig. 13) (k range from 3.7 to 16.0 Å^{-1}, R range from 0.9 to 4.0 Å, E_0 = 6.0 eV, residual ~9.0, N_{ind} = 25, N_{free} = 12). Confidence limits in distances and σ^2 parameters are indicated. Subscript C indicates parameters that were correlated in the refinement.

Type	N	R (Å)	σ^2 (Å^2)
Mo–O	2	67 ± 0.001	00010 ± 0.0001
Mo–O	2	87 ± 0.02	00037 ± 0.0001
Mo–O	1	23 ± 0.004	0.0037_C
Mo–O	1	39 ± 0.003	0.0025 ± 0.0007
Mo–Mo	2	54 ± 0.002	0.0073 ± 0.0009
Mo–Mo	2	72 ± 0.007	0.0073_C
Mo–Mo	2	89 ± 0.015	0.0116 ± 0.001

used did not permit to vary coordination numbers (N) and σ^2 parameters independently. A corresponding fitting procedure resulted in Mo–Mo coordination numbers with very large confidence intervals that exceeded those of the crystallographic bulk structure of reference MoO_3. Hence, for the three Mo–Mo distances used coordination numbers were fixed to the crystallographic values and only σ^2 parameters were refined to account for the reduced amplitude. Clearly, this procedure does not permit to distinguish between particle size effects, morphology, and static disorder. Most likely, even a mixture of these can be expected in the activated MoO_x phase supported on SBA-15. Nevertheless, the number of nearest Mo neighbors at different distances is accurately obtained and can be interpreted.

The first Mo–O shell could be sufficiently simulated using four Mo–O distances. In contrast to Keggin type $PVMo_{11}$ or hex-MoO_3, an increased contribution of Mo–O distances at ~1.67 Å and ~1.87 Å was observed. This contribution originates from the tetrahedral MoO_4 species on the SBA-15 support in addition to the regular distorted MoO_6 units of MoO_3. This result corroborates the interpretation of the increased Mo K pre-edge peak in the XANES spectrum of activated $PVMo_{11}$-SBA-15 in terms of tetrahedral MoO_4 and octahedral MoO_6 units. In total, the activated MoO_x phase that forms at elevated temperatures under reaction conditions corresponded to a mixture of tetrahedrally and octahedrally coordinated MoO_4 and MoO_6 units, respectively. The three Mo–Mo distances required to sufficiently simulate the experimental FT($\chi(k) * k^3$) of activated $PVMo_{11}$-SBA-15 correspond to those characteristic of MoO_3. It may be assumed that the MoO_6 units present exhibit a connectivity similar to that of the building blocks of MoO_3. MoO_4 units may be isolated or connected to other MoO_x units on the surface of SBA-15.

Eventually, XANES and FT($\chi(k) * k^3$) of the Mo oxide species obtained from treatment of $PVMo_{11}$-SBA-15 under reaction conditions (Fig. 12) were compared to those of MoO_x-SBA-15 as reported earlier [11] in Fig. 13. The latter material has been obtained by impregnation of SBA-15 with ammonium heptamolybdate (AHM) followed by calcination and treatment in propene and oxygen at temperatures above 673 K [11]. Despite the poor resolution of the in situ XAS data, it can be seen that electronic (XANES) and geometric (EXAFS) structure of the two differently prepared materials are very similar. Apparently, at elevated temperatures, the particular surface of silica SBA-15 directed the formation of the same supported MoO_x species independent of the polyoxo (AHM) or heteropolyoxo molybdate (Keggin) precursor used. Accordingly, similar catalytic behavior of both activated materials at temperatures above 600 K was observed.

4. Conclusions

Additional metal sites in molybdenum-based selective oxidation catalysts may add functionality and result in further improved catalytic properties. Vanadium containing HPOM supported on SBA-15 appear to be suitable model systems. They would permit to further elucidate correlations between the electronic and geometric structure and the catalytic performance of the resulting mixed oxide catalysts. The structural investigations of as-prepared PMo_{12}-SBA-15 and $PVMo_{11}$-SBA-15 presented here have shown that the respective Keggin ions can be readily supported on silica SBA-15. However, in situ XAS measurements under reducing or oxidizing conditions revealed a pronounced support interaction effect. This effect resulted in a further decreased thermal stability of the supported Keggin ions compared to the bulk materials. Hence, the supported V containing Keggin ion decomposed readily on SBA-15 in contrast to the slow decomposition of bulk HPOM under reaction conditions. Apparently, no stable HPOM Keggin ions could be obtained on silica SBA-15 under reaction conditions. However, in spite of their low thermal stability, preparation of HPOM supported on SBA-15 may be a convenient way to obtain and compare characteristic molybdenum oxide structures supported on SBA-15 with and without additional metal centers. Because preparation of these model systems starts from the same HPOM precursor structure, the resulting activated oxides can be expected to exhibit similar geometric structures regardless of the presence of additional metal centers. This would eventually make the resulting oxides suitable model systems to distinguish between structural and compositional effects on structure activity relationships of molybdenum oxide-based selective oxidation catalysts.

Acknowledgments

The Synchrotron Radiation Laboratories *HASYLAB*, Hamburg, and *ANKA*, Karlsruhe, are acknowledged for providing beamtime for this work. We are grateful to J. Scholz, H. Link, and A. Jürgensen for contributing to the characterization of the materials. The authors acknowledge support from the Deutsche Forschungsgemeinschaft, DFG, and Cluster of Excellence "Unifying Concepts in Catalysis" (DFG).

References

[1] B. Grzybowska-Swierkosz, Top. Catal. 11/12 (2000) 23–42.
[2] R.K. Grasselli, Catal. Today 49 (1999) 141–153.
[3] L. Kihlborg, Acta Chem. Scand. 23 (1969) 1834–1835.
[4] M. Hatano, A. Kayou, United States patent 5049,692, 1991.

[5] T. Ushikubo, K. Oshima, A. Kayou, M. Hatano, Stud. Surf. Sci. Catal. 112 (1997) 473–480.
[6] R.K. Grasselli, D.J. Buttrey, P. DeSanto Jr., J.D. Burrington, C.G. Lugmair, A.F. Volpe, T. Weingand, Catal. Today 91-92 (2004) 251–258.
[7] S. Breiter, M. Estenfelder, H.-G. Lintz, A. Tenten, H. Hibst, Appl. Catal. A 134 (1996) 81–89.
[8] O. Ovsitser, Y. Uchida, G. Mestl, G. Weinberg, A. Blume, J. Jäger, M. Dieterle, H. Hibst, R. Schlögl, J. Mol. Catal. A 185 (2002) 291–303.
[9] T. Ressler, A. Walter, Z.-D. Huang, W. Bensch, J. Catal. 254 (2008) 170–179.
[10] M.M. Lin, Appl. Catal. A: Gen. 207 (2001) 1–16.
[11] T. Okuhara, N. Mizuno, M. Misono, Adv. Catal. 41 (2001) 443–673.
[12] M.E. Davis, C.J. Dillon, J.H. Holles, J. Labinger, Angew. Chem. Int. Ed. 41 (2002) 858–860.
[13] J.H. Holles, C.J. Dillon, J.A. Labinger, M.E. Davis, J. Catal. 218 (2003) 42–53.
[14] J. Wienold, O. Timpe, T. Ressler, Chem.: A Eur. J. 9 (2003) 6007–6017.
[15] T. Ressler, O. Timpe, F. Girgsdies, J. Wienold, T. Neisius, J. Catal. 231 (2005) 279–291.
[16] T. Ressler, O. Timpe, J. Catal. 247 (2007) 231–237.
[17] I.E. Wachs, Catal. Today 100 (2005) 79–94.
[18] K. Chen, S. Xie, A.T. Bell, E. Iglesia, J. Catal. 198 (2001) 232–242.
[19] S.H. Taylor, A.J.J. Pollard, Catal. Today 81 (2003) 179–188.
[20] C. Hess, J. Catal. 248 (2007) 120–123.
[21] D.Y. Zhao, Q.S. Huo, J.L. Feng, B.F. Chmelka, G.D. Stucky, J. Am. Chem. Soc. 120 (1998) 6024.
[22] D.Y. Zhao, J.L. Feng, Q.S. Huo, N. Melosh, G.H. Fredrickson, B.F. Chmelka, G.D. Stucky, Science 279 (1998) 548.
[23] D.E. Keller, B.M. Weckhuysen, D.C. Koningsberger, J. Phys. Chem. B 110 (29) (2006) 14313.
[24] B.M. Weckhuysen, D.E. Keller, Catal. Today 78 (2003) 25.
[25] P. Topka, H. Balcar, J. Rathousky, N. Zilkova, F. Verpoort, J. Cejka, Micropor. Mesopor. Mater. 96 (2006) 44–54.
[26] G. Murali Dhara, G. Muthu Kumarana, Manoj Kumara, K.S. Rawata, L.D. Sharmaa, B. David Rajub, K.S. Rama Rao, Catal. Today 99 (2005) 309–314.
[27] Makoto Misono, Catal. Today 144 (2009) 285–291.
[28] Yuichi Kamiya, Toshio Okuhara, Makoto Misono, Atsuyuki Miyaji, Katsuyuki Tsuji, Tetsuo Nakajo, Catal. Surv. Asia 12 (2008) 101–113.
[29] Heesoo Kim, Ji Chul Jung, In Kyu Song, Catal. Surv. Asia 11 (2007) 114–122.
[30] Andrew D. Newman, D. Robert Brown, Prem Siril, Adam F. Lee, Karen Wilson, Phys. Chem. Chem. Phys. 8 (2006) 2893–2902.
[31] A. Schreiber, I. Ketelsen, G.H. Findenegg, Phys. Chem. Chem. Phys. 3 (2001) 1185–1195.
[32] S. Knobl, Ph.D. Thesis, Technical University Berlin, 2004.
[33] J.-D. Guo, P.Yu. Zavalij, M.S. Whittingham, Eur. J. Solid State Inorg. Chem. 31 (1994) 833–842.
[34] E.P. Barrett, L.G. Joyner, P.P. Halenda, J. Am. Chem. Soc. 73 (1951) 373.
[35] T. Ressler, J. Synch. Rad. 5 (1998) 118–122.
[36] J.J. Rehr, C.H. Booth, F. Bridges, S.I. Zabinsky, Phys. Rev. B 49 (1994) 12347–12350.
[37] J.C.A. Boeyens, G.J. McDougal, J. van Smit, J. Solid State Chem. 18 (1976) 191–199.
[38] T. Ressler, S.L. Brock, J. Wong, S.L. Suib, J. Phys. Chem. B 103 (1999) 6407–6420.
[39] A. Walter, R. Herbert, C. Hess, T. Ressler, Chem. Central J. (2010) 4:3.
[40] <http://www.ixasportal.net/ixas/images/ixas_mat/StandardsCriteria_July25_2000.pdf> (accessed 02.01.10).
[41] Numerical Recipes: The Art of Scientific Computing, third ed., Cambridge University Press, 2007. <http://www.nr.com>.
[42] T. Ressler, A. Walter, J. Scholz, J.-P. Tessonnier, D.S. Su, J. Catal. 271 (2010) 305–314.
[43] T. Ressler, R.E. Jentoft, J. Wienold, T. Neisius, J. Catal. 210 (2002) 67–83.
[44] T. Ressler, J. Wienold, R.E. Jentoft, F. Girgsdies, Eur. J. Inorg. Chem. 2 (2003) 301–312.